ALMA Lensing Cluster Survey: Properties of Millimeter Galaxies Hosting X-Ray-detected Active Galactic Nuclei

Ryosuke Uematsu[1] , Yoshihiro Ueda[1] , Kotaro Kohno[2,3] , Satoshi Yamada[4] , Yoshiki Toba[1,5,6,7] , Seiji Fujimoto[8,9] ,
Bunyo Hatsukade[2] , Hideki Umehata[10,11] , Daniel Espada[12,13] , Fengwu Sun[14] , Georgios E. Magdis[8,9,15] ,
Vasily Kokorev[8,9,16] , and Yiping Ao[17]

[1] Department of Astronomy, Kyoto University, Kyoto 606-8502, Japan; uematsu@kusastro.kyoto-u.ac.jp
[2] Institute of Astronomy, Graduate School of Science, The University of Tokyo, 2-21-1 Osawa, Mitaka, Tokyo 181-0015, Japan
[3] Research Center for the Early Universe, School of Science, The University of Tokyo, 7-3-1 Hongo, Bunkyo-ku, Tokyo 113-0033, Japan
[4] Institute of Physical and Chemical Research (RIKEN), 2-1 Hirosawa, Wako, Saitama 351-0198, Japan
[5] National Astronomical Observatory of Japan, 2-21-1 Osawa, Mitaka, Tokyo 181-8588, Japan
[6] Academia Sinica Institute of Astronomy and Astrophysics, 11F of Astronomy-Mathematics Building, AS/NTU, No.1, Section 4, Roosevelt Road, Taipei 10617,
Taiwan
[7] Research Center for Space and Cosmic Evolution, Ehime University, 2-5 Bunkyo-cho, Matsuyama, Ehime 790-8577, Japan
[8] Cosmic Dawn Center (DAWN), Jagtvej 128, DK-2200 Copenhagen N, Denmark
[9] Niels Bohr Institute, University of Copenhagen, Lyngbyvej 2, DK-2100 Copenhagen Ø, Denmark
[10] Institute for Advanced Research, Nagoya University, Furocho, Chikusa, Nagoya 464-8602, Japan
[11] Department of Physics, Nagoya University, Furo-cho, Chikusa-ku, Nagoya 464-8601, Japan
[12] Departamento de Física Teórica y del Cosmos, Campus de Fuentenueva, Edificio Mecenas, Universidad de Granada, E-18071, Granada, Spain
[13] Instituto Carlos I de Física Teórica y Computacional, Facultad de Ciencias, Campus de Fuentenueva CPE-18071, Granada, Spain
[14] Steward Observatory, University of Arizona, 933 N. Cherry Avenue, Tucson, AZ 85721, USA
[15] DTU-Space, Technical University of Denmark, Elektrovej 327, DK-2800, Kgs. Lyngby, Denmark
[16] Kapteyn Astronomical Institute, University of Groningen, P.O. Box 800, 9700AV Groningen, The Netherlands
[17] Purple Mountain Observatory and Key Laboratory for Radio Astronomy, Chinese Academy of Sciences, Nanjing, People's Republic of China
Received 2022 September 9; revised 2022 December 18; accepted 2023 January 18; published 2023 March 14

Abstract

We report the multiwavelength properties of millimeter galaxies hosting X-ray detected active galactic nuclei (AGNs) from the ALMA Lensing Cluster Survey (ALCS). ALCS is an extensive survey of well-studied lensing clusters with ALMA, covering an area of 133 arcmin^2 over 33 clusters with a 1.2 mm flux-density limit of $\sim$60 μJy (1σ). Utilizing the archival data of Chandra, we identify three AGNs at $z = 1.06$, 2.09, and 2.84 among the 180 millimeter sources securely detected in the ALCS (of which 155 are inside the coverage of Chandra). The X-ray spectral analysis shows that two AGNs are not significantly absorbed ($\log N_{\rm H}/{\rm cm}^{-2} < 23$), while the other shows signs of moderate absorption ($\log N_{\rm H}/{\rm cm}^{-2} \sim 23.5$). We also perform spectral energy distribution modeling of X-ray to millimeter photometry. We find that our X-ray AGN sample shows both high mass-accretion rates (intrinsic 0.5–8 keV X-ray luminosities of $\sim 10^{44-45}\,{\rm erg\,s}^{-1}$) and star formation rates ($\gtrsim 100\,M_\odot\,{\rm yr}^{-1}$). This demonstrates that a wide-area survey with ALMA and Chandra can selectively detect intense growth of both galaxies and supermassive black holes in the high-redshift universe.

Unified Astronomy Thesaurus concepts: Active galactic nuclei (16); X-ray active galactic nuclei (2035); Quasars (1319); Submillimeter astronomy (1647); Galaxy evolution (594); High-redshift galaxies (734); Spectral energy distribution (2129)

1. Introduction

The evolution of galaxies and the supermassive black holes (SMBHs) at their centers is one of the most important issues in modern astronomy. Many studies have shown the tight bulge-mass-to-SMBH-mass correlation in the local universe (e.g., Magorrian et al. 1998; Marconi & Hunt 2003), suggesting the coevolution of SMBHs and the host galaxies. Nevertheless, the large dispersion in the bulge-mass-to-SMBH-mass ratio in high-redshift galaxies (e.g., see Kormendy & Ho 2013 for a review) suggests complexity of the coevolution scenario, and the evolutionary history of individual systems is still unclear.

The average growth rate of galaxies and SMBHs reached a peak at $z = 1$–3, which is often referred to as the *cosmic noon* (e.g., Madau & Dickinson 2014; Ueda et al. 2014, see also Peca

et al. 2023 for a recent study). Thus, galaxies hosting active galactic nuclei (AGNs) at these epochs are a key population to reveal the mechanisms of galaxy-SMBH coevolution. Submillimeter and X-ray observations are powerful tools to study this population. This is because infrared radiation from star formation activity at these redshifts is observed in the millimeter band (submillimeter galaxies; SMGs), while X-ray observations can detect the obscured AGNs. The Atacama Large Millimeter/ submillimeter Array (ALMA) has unprecedentedly high angular resolution and sensitivity in sub/millimeter wavelengths, and has been used extensively to study the high-redshift universe. For example, Wang et al. (2013) found 10 X-ray counterparts to 99 SMGs in the ALMA LABOCA E-CDFS Submillimeter Survey (ALESS; Hodge et al. 2013), from which eight sources were identified as AGNs; hereafter, we refer to these X-ray AGNs as the "ALESS-XAGN" sample. Moreover, Rujopakarn et al. (2016) found six X-ray AGNs from 16 SMGs from the GOODS-S/ultra deep field (UDF) survey (Dunlop et al. 2017); hereafter, "UDF-XAGN". Furthermore, Ueda et al. (2018) identified 13 X-ray

AGNs in a sample consisting of 25 SMGs from the ALMA twenty-Six Arcmin^2 survey of GOODS-S At One-millimeter (ASAGAO; Hatsukade et al. 2018), supplemented by the UDF survey (six X-ray AGNs are the same as UDF-AGN); hereafter, we refer to those X-ray AGNs that are not in the UDF region as "ASAGAO-XAGN". In another case, Umehata et al. (2015) found four X-ray AGNs from eight SMGs of the SSA22 protocluster. Finally, Stach et al. (2019) identified 23 X-ray AGNs from 274 SMGs from the ALMA SCUBA-2 UDS survey (AS2UDS; Stach et al. 2018) falling within the Chandra footprint; hereafter, "AS2UDS-XAGN." These sub/millimeter surveys only cover a limited survey parameter space (depth and area), however. In shallow surveys, the results are biased for intensively star-forming galaxies, whereas rare populations are missed in narrow-area surveys. It is important to conduct deep and wide-area surveys to carry out a complete census of the whole sub/millimeter populations.

Lensed fields are excellent targets to perform deep surveys efficiently. Using ALMA in cycle 6, our team has conducted an extensive survey in high magnification regions of 33 lensing clusters, called the ALMA lensing cluster survey (ALCS; S. Fujimoto et al. 2023, in preparation; K. Kohno et al. 2023, in preparation). The sample comes from the best-studied clusters of galaxies observed with the Hubble Space Telescope (HST) treasury programs, i.e., CLASH (Postman et al. 2012), Hubble Frontier Fields (HFF; Lotz et al. 2017; Steinhardt et al. 2020), and RELICS (Coe et al. 2019). The total survey area is 133 arcmin^2 and the depth is $\sim$60 μJy (1.2 mm, 1σ). The ALCS achieves, after correcting for lensing, one of the widest and deepest millimeter surveys among ALMA unbiased surveys conducted to date (S. Fujimoto et al. 2023, in preparation).

In this paper, we investigate the properties of the three millimeter galaxies hosting X-ray detected AGNs in the ALCS, using the archival data of Chandra. It should be noted here that while clusters are good fields for submillimeter observations, they are a challenging space for X-ray observation because of the bright diffuse emission of clusters (e.g., Fabian et al. 2000). We estimate the X-ray luminosities (or mass-accretion rates), star formation rates (SFRs), and stellar masses of this sample, and discuss their evolutionary stages in comparison with other X-ray detected samples.

The structure of this paper is as follows. In Section 2, we describe the details of sample selection and data reductions. Section 3 presents the X-ray spectral analysis and the spectral energy distribution (SED) modeling. Sections 4 and 5 are the discussion and conclusion, respectively. Throughout the paper, we assume a flat universe with $H_0 = 70.4$ km s^{-1} Mpc^{-1} and $\Omega_M = 0.272$ (Komatsu et al. 2011). The Chabrier initial mass function (IMF; Chabrier 2003) is adopted.

2. Observations and Data Reduction

2.1. Observations and Source Detection with ALMA

ALMA Band 6 observations of the 33 lensing clusters were conducted between 2018 December and 2019 December through the program 2018.1.00035.L (PI: K. Kohno; K. Kohno et al. 2023, in preparation) with a 15 GHz total bandwidth covering 250.0–257.5 and 265.0–272.5 GHz. Two compact array configurations (C43-1 and C43-2) were used to obtain a moderate synthesized beam size ($\sim$1$''$) to avoid losing sensitivity for spatially extended sources, which can be expected for highly magnified cases. For five HFFs, we also combined the existing

ALMA data from 2013.1.00999S and 2015.1.01425.S (PI: F. Bauer; González-López et al. 2017a, 2017b).

All the ALMA data were calibrated and reduced with the Common Astronomy Software Applications package (CASA; McMullin et al. 2007) with the pipeline script in the standard manner. Different pipeline versions were used for observations obtained in different cycles, i.e., v5.4.0 for 26 clusters observed in Cycle 6 and v5.6.1 for the remaining clusters in Cycle 7. The naturally weighted 1.15 mm continuum images have a typical noise level of $\sim$60 μJy beam^{-1} with a native beam size of $\sim$1$''$ with the natural weighting. We also produced lower-resolution maps by applying a uv taper, yielding a typical beam size of $\sim$2$''$, which is better suited for spatially elongated, low surface brightness emission.

The continuum sources were extracted from the native and tapered maps with the natural weighting using SExtractor v2.5.0 (Bertin & Arnouts 1996). Details of the ALMA data analysis, source extraction processes, and the ALCS 1.2 mm continuum source catalog will be presented in a separate paper (S. Fujimoto et al. 2023, in preparation).

2.2. Chandra Counterparts

Chandra (Weisskopf et al. 2002) has observed the ALCS fields on multiple occasions since 1999 with the Advanced CCD Imaging Spectrometer (ACIS; Garmire et al. 2003). It covers all the ALCS fields except for RXC J0032.1+1808 and RXC J0600.1-2007, with a median exposure of $\sim$80 ks, 55 sources out of the 180 secure ALCS sources are covered by the existing Chandra data. We processed all the data obtained by 2017, following the standard analysis procedures with the Chandra interactive analysis of observations (CIAO v4.12) software and calibration database (CALDB v4.9.1). The products were combined by using merge_obs and sources were detected by running wavdetect (Freeman et al. 2002) in the 0.5–7.0 keV band. In the detection, the false-positive probability threshold was set to 10^{-8} and the wavelet scales were set to a $\sqrt{2}$ $sequence$ (i.e., 1, $\sqrt{2}$, 2, 2$\sqrt{2}$, 4, $\sqrt{2}$, 8, 8$\sqrt{2}$, and 16 pixels), which are the same settings as used in Luo et al. (2008). We cross-matched the Chandra detected sources with the secure ALCS source list comprising 180 millimeter detected galaxies (see S. Fujimoto et al. 2023, in preparation). The X-ray counterpart of an ALMA source was identified if the position coincides with the ALMA position within the Chandra positional uncertainty, for which we adopt the root sum square of the 3σ statistical error and the 99% absolute astrometry uncertainty of Chandra (1$''$4).[18] We ignored the positional uncertainty of ALMA, which is much smaller than that of Chandra. The cluster center regions are excluded because of the difficulty in identifying point sources.

The three X-ray counterparts were found in the cluster fields of Abell370, MACSJ0416.1-2403, and MACS0329.7-0211, where the total exposure times of the Chandra observations are 96.3, 328, and 77.5 ks, respectively. The source names are A370-ID110, M0416-ID117, and M0329-ID11 (hereafter "ALCS-XAGN"). Their coordinates are summarized in Table 1. We extracted the X-ray spectra from circular regions with radii of 1$''$5 for A370-ID110 and 2$''$0 for M0416-ID117 and M0329-ID11[19] centered at the X-ray source positions, and

---

[19] Since the point-spread function size at M0416-ID117 and M0329-ID11 is slightly larger than that at A370-ID110, we adopted a little larger aperture for the former two sources.

Table 1
Physical Properties of the AGNs and Their Host Galaxies

Name	R.A. (degree)	Decl. (degree)	z	μ	$N_{\rm H}$ (10^{22} cm^{-2})	Γ	$\log L_{\rm X}$ (erg s^{-1})	log SFR ($M_\odot$ yr^{-1})
(1)	(2)	(3)	(4)	(5)	(6)	(7)	(8)	(9)
$\log M_*$ ($M_\odot$)	$\log L_{\rm dust}$ ($L_\odot$)	$\log M_{\rm dust}$ ($M_\odot$)	$U_{\rm min}$	IRX	β	$f_{\rm AGN}$	$\log L_{\rm IR}$ ($L_\odot$)
(10)	(11)	(12)	(13)	(14)	(15)	(16)	(17)
A370-ID110	39.985689	−1.5739784	1.06	1.19	$32.8^{+11.7}_{-10.6}$	$2.5^{+0.8}_{-0.8}$	$45.0^{+0.7}_{-0.5}$	2.43 ± 0.02
11.81 ± 0.06	12.51 ± 0.02	8.80 ± 0.02	25.0 ± 0.4	2.14 ± 0.02	0.49 ± 0.13	0.23 ± 0.09	12.68
M0416-ID117	64.0449843	−24.0798771	2.09	1.57	$2.4^{+8.6}_{-2.4}$	$2.1^{+0.9}_{-0.6}$	$43.8^{+0.6}_{-0.3}$	1.93 ± 0.05
10.81 ± 0.16	12.01 ± 0.03	7.98 ± 0.11	51.2 ± 12.5	0.84 ± 0.03	-1.85 ± 0.02	0.05 ± 0.01	12.07
M0329-ID11	52.4239873	−2.1824407	2.84	2.46	$0.1^{+5.9}_{-0.1}$	$1.7^{+0.6}_{-0.4}$	$44.4^{+0.3}_{-0.2}$	2.18 ± 0.08
10.74 ± 0.21	11.77 ± 0.15	8.63 ± 0.15	7.3 ± 3.7	-0.03 ± 0.14	-2.03 ± 0.08	0.55 ± 0.22	12.40

Note. (1) Source names. (2) and (3) ALMA source position. (4) Redshift. Those of A370-ID110 and M0416-ID117 are the spectroscopic redshifts, while that of M0329-ID11 is the photometric redshift (see Section 3.1 for more details). (5) Magnification factor due to the lensing effect (S. Fujimoto et al. 2023, in preparation). (6) X-ray absorption hydrogen column density in units of 10^{22} cm^{-2}. (7) Photon index. (8) Intrinsic X-ray luminosity in the rest-frame 0.5–8.0 keV band. (9) SFR. (10) Stellar mass. (11) Total infrared emission from interstellar dust. (12) Dust mass. (13) Minimum radiation field illuminating the interstellar dust. (14) Infrared excess (IRX $= \log L_{\rm dust}/L_{\rm UV}$). In CIGALE, IRX is calculated from the GALEX far-UV (FUV) filter and dust luminosity. (15) Power-law index of the observed UV slope, which is measured in the same way as Calzetti et al. (1994) did. (16) Fraction of AGN IR luminosity to total IR luminosity, where we use the rest-flame 8–1000 μm luminosities. (17) IR luminosity in the rest-frame 8–1000 μm band, which is measured by integrating the best-fit SED over a wavelength of 8–1000 μm. Errors attached in (6)–(8) correspond to the 90% confidence regions, whereas those in (9)–(16) show the 1σ confidence regions. All physical quantities in this table are corrected for the lensing magnification; possible uncertainties in the magnification factors are ignored. Because of the poor far-infrared data of M0329-ID11, the IR luminosity may have a large uncertainty.

subtracted the backgrounds taken from source-free regions around the objects.

It should be noted that these AGNs have also been reported in previous studies. A370-ID110 was first discovered by the submillimeter survey of Abell 370 using the Submillimeter Common-User Bolometer Array (SCUBA; Smail et al. 1997), and was subsequently detected in X-rays by a Chandra follow-up (Bautz et al. 2000). Its properties have been discussed in several papers (e.g., Soucail et al. 1999; Smail et al. 2002; Alexander et al. 2005). M0416-ID117 was previously detected by ALMA in González-López et al. (2017b), and its physical properties were discussed in Laporte et al. (2017). M0416-ID117 and M0329-ID11 were detected in blind X-ray surveys using Chandra archival data by Wang et al. (2016) and Gilmour et al. (2009), respectively. In this paper, we reanalyze the X-ray spectra and then perform X-ray to millimeter SED analyses utilizing the newly obtained ALMA data.

2.3. HST, Spitzer, and Herschel Counterparts

Optical, near-infrared, and mid-infrared images of these three clusters with the ALCS-XAGNs have been taken using HST ACS and WFC3, and Spitzer Space Telescope (Spitzer) IRAC (Fazio et al. 2004). The images and source catalogs were built by reprocessing available archival HST and Spitzer/IRAC 3.6 and 4.5 μm mosaics of ALCS fields (Kokorev et al. 2022). All three ALCS-XAGN sources have counterparts in ACS, WFC3, and IRAC (channels 1 and 2) images as shown in Figure 1. We also utilized IRAC (channels 3 and 4) and MIPS (Rieke et al. 2004) photometric data from the Spitzer Enhanced Imaging Products (SEIP; SSC & IRSA 2020). Only the counterpart of A370-ID110 was found in the SEIP catalog within 1″5. M0416-ID117 and M0329-ID11 were found outside the coverage of IRAC ch3, ch4, and MIPS.

Herschel Space Observatory (Herschel) PACS and SPIRE images at 100–500 μm bands have been obtained for the ALCS fields (mostly through the Herschel Lensing Survey; Egami et al. 2010; Sun et al. 2021). One of the fields, Abell 370 has

been observed as part of the PACS Evolutionary Probe (PEP; Lutz et al. 2011). Although some of the ALCS fields have only shallow (*snapshot*) SPIRE coverages without PACS observations, all three ALCS-XAGN containing fields have deep SPIRE and PACS images. The PACS 100 μm images of these three ALCS-XAGN sources are also presented in Figure 1. Details of the Herschel data in ALCS fields have been described in Sun et al. (2022).

3. Spectral Analysis and Results

3.1. X-Ray Spectral Analysis

We fit the observed (magnification not corrected) X-ray spectra with a simple absorbed power-law model. This model is represented as follows in the XSPEC (Arnaud 1996) terminology:

$$\text{phabs} * \text{zphabs} * \text{zpowerlaw}. \tag{1}$$

The first term (phabs) represents the galactic photoelectric absorption and the second term (zphabs) an intrinsic absorption at the source redshift. All the parameters are left as free parameters except for the galactic absorption column density and the redshift. The former is fixed at the values estimated by the method of Willingale et al. (2013). The redshifts are fixed at the spectroscopic ones obtained by Canada–France–Hawaii Telescope in A370-ID110 ($z = 1.06$; Soucail et al. 1999) and the Grism Lens-Amplified Survey from Space in M0416-ID117 ($z = 2.09$; Hoag et al. 2016), and at the photometric one estimated by the optical to near-infrared SED analysis with the EAZY code in M0329-ID11 ($z = 2.84^{+0.10}_{-0.11}$; Kokorev et al. 2022).

We are able to adequately reproduce the X-ray spectra of the AGNs, with reduced chi-square values of less than 1 ($\chi^2/\text{dof} < 1$). The left panels of Figure 2 show the result of the X-ray spectral fitting. The best-fit parameters are summarized in Table 1. A370-ID110 shows a significant absorption in
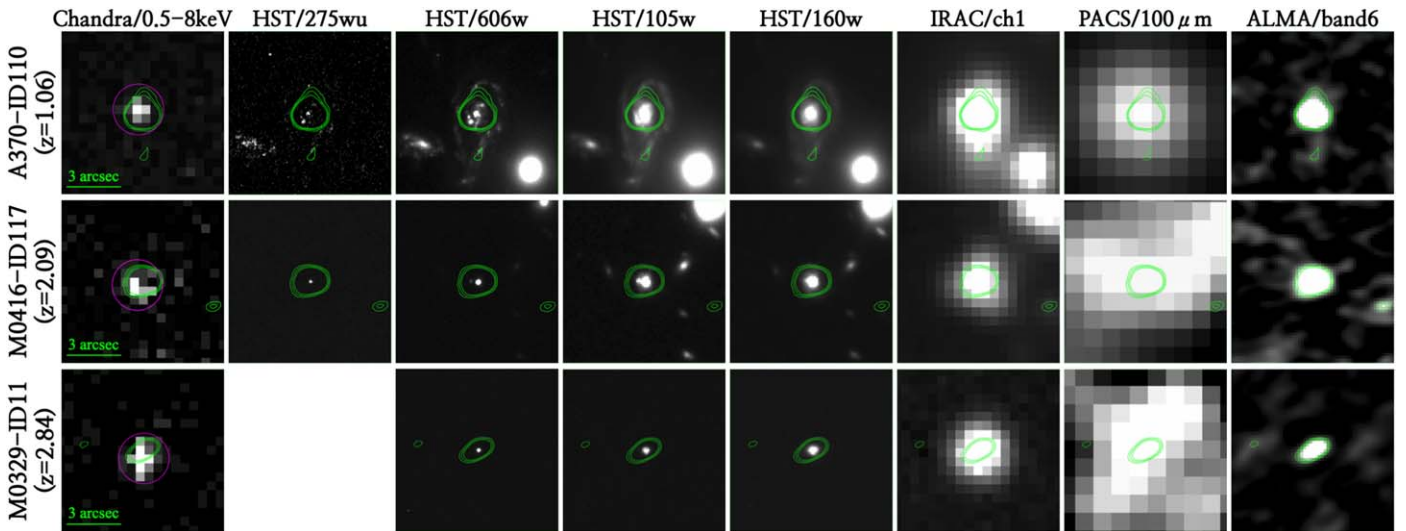
Figure 1. Multiwavelength images of the ALCS-XAGNs. The green contours show the intensity in the ALMA band drawn at 1σ intervals from 3σ–5σ. The magenta circles in the Chandra images show the absolute astrometry uncertainty of Chandra ($1\rlap.{''}4$). For the three sources, the statistical error of Chandra is much smaller than the absolute one ($<0\rlap.{''}3$). The Herschel/PACS images are smoothed with 2D Gaussians of σ radii of 1.5 pixels.

the X-ray spectrum. This is consistent with the previous X-ray study by Bautz et al. (2000). We note that A370-ID110 and M0329-ID11 show especially high X-ray luminosities ($\log L_{\rm X}/{\rm erg\ s}^{-1} \gtrsim 44.5$) compared with normal AGNs.

3.2. SED Modeling with CIGALE

We perform multicomponent SED modeling of the X-ray to millimeter photometry, where we use the magnification-corrected photometries. We employ the latest version of Code Investigating GALaxy Emission (CIGALE v2022.0; Burgarella et al. 2005; Noll et al. 2009; Boquien et al. 2019; Yang et al. 2020, 2022) to conduct X-ray to millimeter SED modeling by self-consistently considering the energy balance between the UV/optical and IR. The SED modules used for the fitting are as follows. We employ a delayed star formation history (SFH) model, assuming a single starburst with an exponential decay. The simple stellar population (SSP) is modeled with the stellar templates of Bruzual & Charlot (2003), where we assume the Chabrier (2003) IMF. We apply a modified Calzetti starburst attenuation law (Calzetti et al. 2000), where we also allow a steeper curve than the original one. The standard nebular emission model (see Inoue 2011) is also added. For the AGN emission, we adopt the SKIRTOR model (Stalevski et al. 2012, 2016), a clumpy two-phase torus model. The dust emission is modeled by the dust templates of Jones et al. (2017). We assume an isotropic X-ray radiation from an AGN, where we fix the photon index of 1.9 as a common value, which is well within the errors derived by the X-ray spectral analysis. Here, we use the 2–8 keV absorption corrected flux derived by the X-ray spectral analysis.[20] The redshifts are fixed at the values noted in Section 3.1. The free parameters are summarized in Appendix appendix. The physical properties are estimated by the Bayesian method, where we adopt log-uniform distributions for the prior probability distributions of the SFR,[21] stellar mass (M_*), dust luminosity ($L_{\rm dust}$), and dust mass($M_{\rm dust}$),[22]

while uniform distributions are assumed for those of minimum radiation field of interstellar dust ($U_{\rm min}$), infrared excess ($\mathrm{IRX} = \log L_{\rm dust}/L_{\rm UV,SF}$), and power-law index of observed UV slope (β).

We confirm that CIGALE successfully reproduces the SEDs from millimeter to X-ray of all the sources ($\chi^2/{\rm dof} < 5$).[23] The right panels of Figure 2 show the results of the SED modeling. The physical properties are summarized in Table 1. The SED analysis suggests that A370-ID110 is a type 2 AGN, whereas M0416-ID117 and M0329-ID11 are type 1 AGNs. This result is consistent with the AGN types suggested by the X-ray absorption hydrogen column densities (type 1: $\log N_{\rm H}/{\rm cm}^2 \lesssim 22$, type 2: $\log N_{\rm H}/{\rm cm}^2 \gtrsim 22$). We also confirm that the near-infrared spectrum of A370-ID110 (Takata et al. 2006) shows no clear broad emission lines. We find that all the sources are classified as ultraluminous infrared galaxies ($L_{\rm IR}/L_\odot > 10^{12}$) and show high SFRs (SFR $\gtrsim 100\ M_\odot\ {\rm yr}^{-1}$). This is consistent with the results presented in Sun et al. (2022). We also confirm that the physical properties of A370-ID110 and M0416-ID117 are consistent with those reported in previous studies (Smail et al. 2002; Laporte et al. 2017).

4. Discussion

We discuss our results in comparison with other ALMA and Chandra-selected AGN samples (i.e., ALESS-XAGN, UDF-XAGN, ASAGAO-XAGN, and AS2UDS-XAGN) at $z = 1$–3. We also compare our results with X-ray-selected broad line AGNs at $z = 1.18$–1.68 in the SXDF (hereafter, SXDF-XAGN; Ueda et al. 2008) as a sample with a different selection method. The stellar masses and SFRs of ALESS-XAGNs, UDF-XAGNs, ASAGAO-XAGNs, and AS2UDS-XAGN are estimated by the MAGPHYS code (da Cunha et al. 2015; Yamaguchi et al. 2020; Dudzevičiūtė et al. 2020), while those of SXDF-XAGNs are estimated by the X-CIGALE code (Setoguchi et al. 2021). The X-ray luminosities

---

[20] We adopt the average of the upper and lower errors as the flux error.
[21] In this paper, the term "SFR" refers to the average star formation rate in the last 10 Myr.
[22] In this paper, we use the terms *dust luminosity* and *dust mass* to describe those of interstellar dust (i.e., not including those in the AGN torus).

[23] Although this threshold is much larger than in an ordinary chi-square test, we adopt a conservative value by considering an oversimplification of the SED model, such as the SFH profile, ignorance of time variability in AGN, and uniform distribution of interstellar dust among stars (see, e.g., Toba et al. 2022).
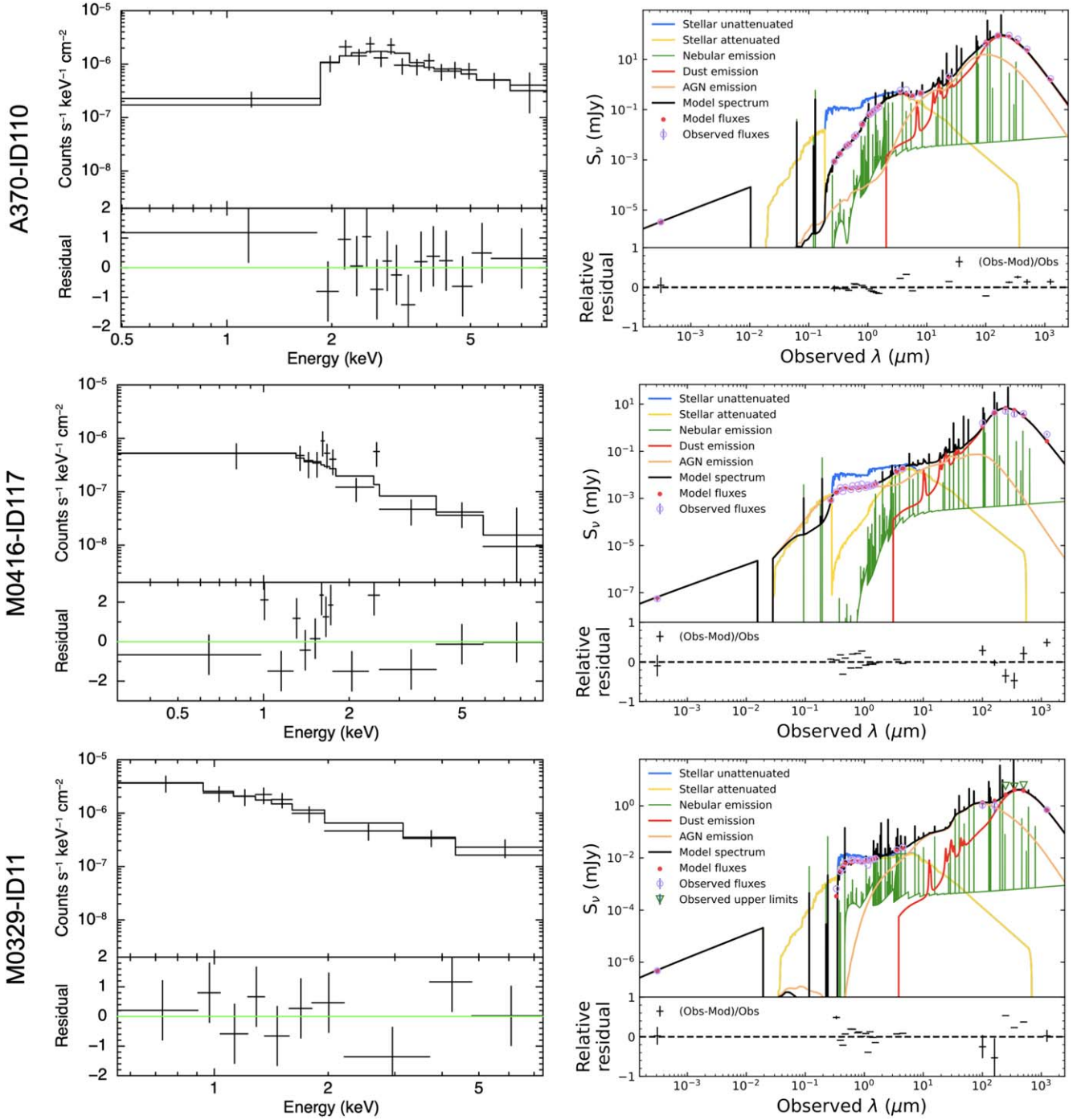
Figure 2. Left: folded X-ray spectra corrected for the effective area and the best-fit models of the ALCS-XAGNs. The lower panel shows the residuals. Right: results of the SED modeling. The solid black line represents the best-fit SEDs. The lower panel shows the residuals. The X-ray spectra are not corrected for lensing magnification, while the X-ray to millimeter SEDs are corrected.

of ALESS-XAGNs, UDF-XAGNs, ASAGAO-XAGNs, and AS2UDS-XAGNs are taken from Wang et al. (2013), Ueda et al. (2018), and Kocevski et al. (2018), respectively. We also extract the X-ray luminosities of SXDF-XAGNs from Nobuta et al. (2012), where we convert the 2–10 keV luminosity to 0.5–8 keV luminosity, assuming a power-law spectrum with $\Gamma = 1.9$. Here we note that all the X-ray luminosities of AS2UDS-XAGNs and ALESS-AGNs are estimated at their spectroscopic redshifts, while the stellar masses and SFRs are estimated at their photometric ones. In this paper, we only plot the sources whose photometric redshifts are close to their

spectroscopic ones within $-0.3 < (z_{\mathrm{photo}} - z_{\mathrm{spec}})/(1 + z_{\mathrm{spec}}) < 0.3$. Hence, the systematic errors in stellar masses and SFRs are estimated to be ~ 0.3 dex, which does not affect our discussions.

Recently, Hunt et al. (2019) investigated the systematic differences among the three SED models: GRASIL (Silva et al. 1998), MAGPHYS, and CIGALE, utilizing the FUV to submillimeter SEDs of the 61 galaxies from the KINGFISH sample (Kennicutt et al. 2011). They have shown that galaxies with high specific SFRs ($\log \mathrm{sSFR}[\mathrm{yr}^{-1}] > -10.6$) show good agreement in their stellar masses and SFRs among the three
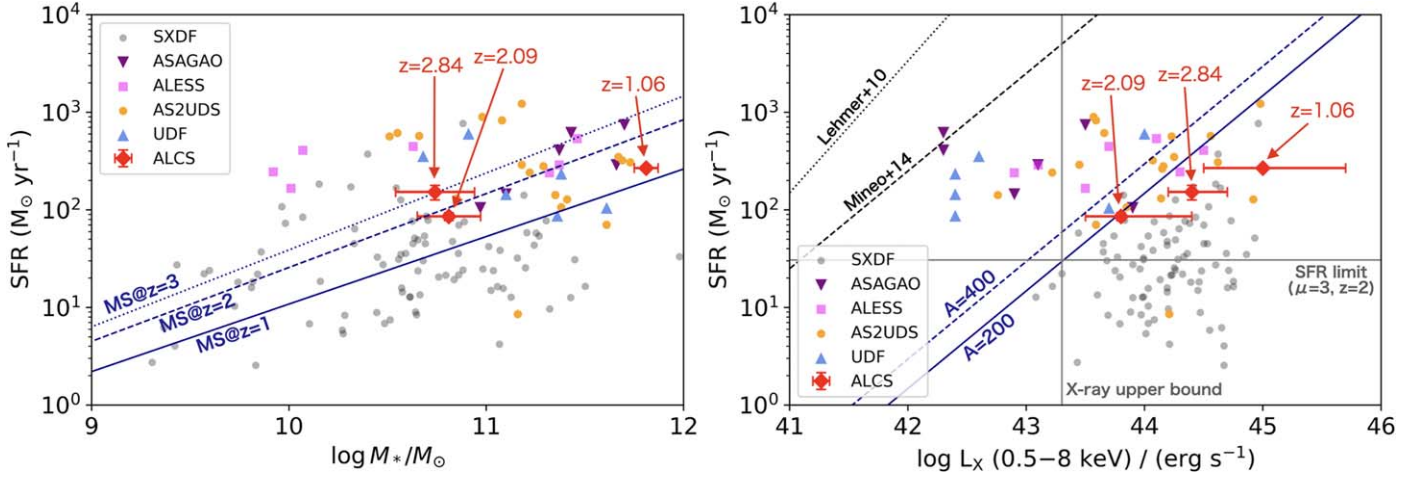
Figure 3. Left: stellar masses (M_*) vs. SFRs. The blue lines represent the star-forming *main sequence* at $z = 1.0$ (solid), $z = 2.0$ (dashed), and $z = 3.0$ (dotted), respectively (Speagle et al. 2014). Right: de-absorbed X-ray luminosities vs. SFRs. The solid and dashed blue lines represent the relation of galaxy-SMBH simultaneous evolution for $A = 200$ and 400, respectively (Section 4.2). All the physical quantities in this figure are corrected for lensing magnification. For comparison, we show the X-ray contribution from star formation activity with dotted (Lehmer et al. 2010) and dashed (Mineo et al. 2014) black lines. We also show the median X-ray upper bounds of Chandra non-detected ALCS sources with the vertical gray line, where we assume an intrinsic X-ray absorption of $\log N_{\mathrm{H}}/\mathrm{cm}^{-2} = 23$ (R. Uematsu et al. 2023, in preparation). Moreover, we show the detection limit of SFR with the horizontal gray line. The SFR limit is converted from the infrared luminosity limit by assuming the Kennicutt law (Kennicutt 1998), where we multiply 0.63 to correct the Salpeter IMF to the Chabrier IMF. The infrared luminosity limit is estimated from the observed flux limit at 1.2 mm ($\sim$300 μJy; 5σ) by assuming a single graybody with an emissivity index of 1.8 and temperature of 35 K at $z = 2$, using a typical magnification factor of 3.

models, whereas those with low sSFRs sometimes show large differences in their SFRs. The sSFRs of the ALESS-XAGNs, UDF-XAGNs, ASAGAO-XAGNs, and AS2UDS-XAGNs are adequately high ($\log \mathrm{sSFR}[\mathrm{yr}^{-1}] > -9.6$), and hence we ignore the systematic difference between CIGALE and MAGPHYS as an approximation.[24]

4.1. Stellar Mass versus SFR

The left panel of Figure 3 shows stellar masses versus SFRs for our three sources and other AGN samples (ALESS-XAGN, UDF-XAGN, ASAGAO-XAGN, AS2UDS-XAGN, and SXDF-XAGN). We also show the star-forming *main sequence* at $z = 1.0$, 2.0, and 3.0 given by Speagle et al. (2014). Our sample is distributed close to the main-sequence lines (within 0.2 dex along the SFR axis). This indicates that our sources are normal star-forming galaxies at $z = 1$–3, i.e., galaxies with no clear evidence for negative feedback by the AGNs. We note that the ALCS-XAGN sample contains a massive star-forming galaxy (A370-ID110; $M_* > 10^{11} M_\odot$) and that the SFRs of ALCS-XAGN tend to be smaller than those of the compared SMG samples (see the next section).

4.2. X-Ray Luminosity versus SFR

The right panel of Figure 3 shows X-ray luminosities versus SFRs. We also show the relation of galaxy-SMBH simultaneous evolution for the local M_{BH}-versus-M_{bulge} and M_{BH}-versus-M_{stellar} relations. This relation is given as

$$\mathrm{SFR} * (1 - R) = A \times \dot{M}_{\mathrm{BH}}, \qquad (2)$$

where R is the return fraction ($R = 0.41$ for a Chabrier IMF), and A is the mass ratio ($M_{\mathrm{bulge}}/M_{\mathrm{BH}} = 200$ and $M_{\mathrm{stellar}}/M_{\mathrm{BH}} = 400$; see Ueda et al. 2018 for more details). The mass-accretion

rate can be estimated by the X-ray luminosity as

$$\dot{M}_{\mathrm{BH}} = \kappa_{0.5-8} L_{\mathrm{X}} (1 - \eta)/(\eta c^2), \qquad (3)$$

where $\kappa_{0.5-8}$ is the bolometric correction factor ($\kappa_{0.5-8} = 13$ or $\kappa_{2-10} = 20$ assuming a photon index of 1.9; Vasudevan & Fabian 2007), η is the radiation efficiency ($\eta = 0.05$), and c is the speed of light. ALCS-XAGNs are located on the *simultaneous evolution* line or in the AGN-dominant phase, while the other ALMA and Chandra-selected samples belong to the star formation-dominant phase. This is a unique feature of our ALCS-XAGN sample among sub/millimeter-selected galaxies, realized by the following selection effects. Since the X-ray data of ALCS are shallower but cover a wider area than those of the UDF survey and ASAGAO, high X-ray luminosity (hence rare) AGNs can be efficiently selected in the ALCS sample. On the other hand, because ALCS is much deeper than the parent sample of ALESS and AS2UDS,[25] whose median SFRs are $\sim$250 $M_\odot$ yr^{-1}, ALCS can detect AGNs in the AGN-dominant phase, which are relatively faint in the millimeter band with SFRs $\lesssim$ 250 $M_\odot$ yr^{-1}. Besides, since the ALCS-XAGNs are selected by millimeter observations, they are more biased to higher SFRs compared with purely X-ray-selected AGN samples (e.g., SXDF-XAGNs whose median SFR is $\sim$30 $M_\odot$ yr^{-1}). Page et al. (2012) showed that SMGs containing AGNs with high mass-accretion rates show relatively low SFRs, implying negative feedback by the AGNs. Given this trend, A370-ID110 and M0329-ID11, which show both high SFRs (SFR $> 100 M_\odot$ yr^{-1}) and high X-ray luminosities ($\log L_{\mathrm{X}}/\mathrm{erg}\,\mathrm{s}^{-1} \gtrsim 44.5$), may be a rare population that is

---

[24] The systematic difference between CIGALE and MAGPHYS in the ALCS sample will be discussed in a forthcoming paper on the SED analysis of all the ALCS sources (R. Uematsu et al. 2023, in preparation).

[25] Since ALESS and AS2UDS are follow-up observations of the single-dish surveys LESS (Weiß et al. 2009) and S2CLS (Geach et al. 2017), respectively, their properties are basically determined by the selection bias of the parent samples.

difficult to have been detected in previous sub/millimeter surveys.

According to the merger-driven evolutionary scenario proposed by many authors (e.g., Sanders & Mirabel 1996; Hopkins et al. 2008; Yamada et al. Yamada 2021, 2023; Yutani et al. 2022), the galaxies and SMBHs *coevolve* during major mergers being deeply embedded by gas and dust, and then evolve to the AGN-dominant phase with quenched SFRs by AGN feedback. If this scenario is applicable, our sources may correspond to the transition stage where the merging has finished, but the star formation is not yet quenched. The smaller obscuration in our AGNs than that in late-stage mergers (Ricci et al. 2017, 2021; Yamada et al. 2021) is also consistent with this picture. We note, however, that it is not clear whether the AGNs and star formation activities in our sample are indeed triggered by merger processes or not. Some studies argue that a significant fraction of AGNs at $z \sim 1$–3 are triggered by secular mechanisms (e.g., Schawinski et al. 2011; Kocevski et al. 2012; Draper & Ballantyne 2012), where star formation activities may inject turbulence in the gas disks and make the gas fall into the nuclear regions (Hobbs et al. 2011). Given the high SFRs of ALCS-XAGNs, the AGN activities might be triggered by the intense star formation activities in their host galaxies. Fujimoto et al. (2018) studied the morphology of dusty star-forming galaxies detected in ASAGAO at $z = 1$–3. They found that the ULIRGs at $z = 1$–3 showed larger fractions of irregular and merging galaxies than less luminous galaxies, implying the significant contribution of the ongoing merger process in high-redshift ULIRGs, although the fraction of disk galaxies is the largest even in the ULIRG sample. In our X-ray AGN sample, only A370-ID110 is confirmed to have disk-like structure, while M0416-ID117 and M0329-ID11 are too faint to examine their morphology. Future investigation of host galaxy morphology with JWST or the Thirty Meter Telescope would be helpful to reveal the origins of the high mass-accretion rates and SFRs in our sample.

5. Conclusions

We have reported the multiwavelength properties of millimeter galaxies hosting AGNs detected in the ALCS. The main conclusions are summarized as follows:

1. Utilizing the archival data of Chandra, we have identified three AGNs out of the 180 millimeter galaxies securely detected in the ALCS, which are found in the fields of Abell370, MACSJ0416.1-2403, and MACS0329.7-021 at spectroscopic redshifts of 1.06 and 2.09, and photometric redshift of 2.84, respectively.
2. The X-ray spectral analysis shows that two AGNs are not significantly absorbed ($\log N_{\mathrm{H}}/\mathrm{cm}^{-2} < 23$), while one shows signs of moderate absorption ($\log N_{\mathrm{H}}/\mathrm{cm}^{-2} \sim 23.5$).
3. We have performed SED modeling of the X-ray to millimeter photometry with the CIGALE code. We find that our sources have both high mass-accretion rates (intrinsic

0.5–8 keV X-ray luminosities of $\sim 10^{44-45}\,\mathrm{erg\,s^{-1}}$) and SFRs ($\gtrsim 100 M_\odot\,\mathrm{yr}^{-1}$).

4. We find that ALCS-XAGNs show higher mass-accretion rates than other ALMA-selected X-ray AGN samples. We also confirm that ALCS-XAGNs show higher SFRs than a purely X-ray-selected AGN sample. This can be explained by the selection bias, showing that a wide and deep survey with ALMA, combined with medium-depth X-ray data, can efficiently detect an intense growth stage of both galaxies and SMBHs in a high-redshift universe.

Appendix
Parameters Used in the SED Analysis

Table 2 summarizes the free parameters used in the SED modeling. Each SED module is explained in Section 3.2.

Table 2
Parameter Ranges Used in the SED Modeling with CIGALE

Parameter	Symbol	Value
SFH (Delayed SFH)		
e-folding time of the main stellar population	τ_{main} [Myr]	300, 600, 1000, 3000, 5000, 7000, 9000
Age of the main stellar population	$\mathrm{age}_{\mathrm{main}}$ [Myr]	300, 600, 1000, 2000, 3000, 4000, 5000
SSP (bc03; Bruzual & Charlot 2003)		
IMF of the stellar model		Chabrier (2003)
Metallicity of the stellar model		0.02
Dust Attenuation (dustatt_modified_starburst; Calzetti et al. 2000)		
The color excess of the nebular lines.	$E(B-V)_{\mathrm{lines}}$	0.05, 0.1, 0.15, 0.2, 0.4, 0.6, 0.8, 1.0, 1.2, 1.4, 1.6, 1.8, 2.0, 2.2, 2.4
Reduction factor to apply $E(B-V)_{\mathrm{lines}}$ to calculate the stellar continuum attenuation	$E(B-V)_{\mathrm{factor}}$	0.44
Power-law index to modify the attenuation curve	δ	$-0.6, -0.3, 0.0$
AGN Emission (skirtor2016; Stalevski et al. 2012, 2016)		
Average edge-on optical depth at 9.7 μm	$\tau_{9.7}$	3, 7, 11
Radial gradient of dust density	p	1.0
Dust density gradient with polar angle	q	1.0
Half-opening angle of the dust-free cone	Δ [°]	40
Ratio of the outer to the inner radius	R	20
Inclination	θ [°]	30, 60
Fraction of AGN IR luminosity to total IR luminosity	f_{AGN}	0.1, 0.3, 0.5, 0.7, 0.9
Extinction in the polar direction	$E(B-V)_{\mathrm{pol}}$	0.0, 0.1, 0.8
Temperature of the polar dust	T_{pol} [K]	100, 200
Dust Emission (Themis; Jones et al. 2017)		
Mass fraction of small hydrocarbon solids	q_{PAH}	2.5
Minimum radiation field	U_{min}	1, 5, 10, 25, 50
Power-law index of the starlight intensity distribution	α	2.0, 2.5
Fraction of dust illuminated from U_{min} to U_{max}	γ	0.01, 0.05, 0.1
X-Ray emission		
Photon index	Γ	1.9
Maximum deviation of α_{ox} from the empirical relation[a]		0.2

Note.

[a] We adopt the well-studied "α_{ox}-$L_{2500\,\text{Å}}$" relation, where α_{ox} is defined as $\alpha_{\mathrm{ox}} \equiv -0.3838 \times \log(L_{2500\,\text{Å}}/L_{2\mathrm{keV}})$ and the empirical relation is written as $\alpha_{\mathrm{ox}} = -0.137 \log(L_{2500\text{Å}}) + 2.638$ (Just et al. 2007).

ORCID iDs

Ryosuke Uematsu ⓘ https://orcid.org/0000-0001-6653-779X
Yoshihiro Ueda ⓘ https://orcid.org/0000-0001-7821-6715
Kotaro Kohno ⓘ https://orcid.org/0000-0002-4052-2394
Satoshi Yamada ⓘ https://orcid.org/0000-0002-9754-3081
Yoshiki Toba ⓘ https://orcid.org/0000-0002-3531-7863
Seiji Fujimoto ⓘ https://orcid.org/0000-0001-7201-5066
Bunyo Hatsukade ⓘ https://orcid.org/0000-0001-6469-8725
Hideki Umehata ⓘ https://orcid.org/0000-0003-1937-0573
Daniel Espada ⓘ https://orcid.org/0000-0002-8726-7685
Fengwu Sun ⓘ https://orcid.org/0000-0002-4622-6617
Georgios E. Magdis ⓘ https://orcid.org/0000-0002-4872-2294
Vasily Kokorev ⓘ https://orcid.org/0000-0002-5588-9156
Yiping Ao ⓘ https://orcid.org/0000-0003-3139-2724

References

Alexander, D. M., Bauer, F. E., Chapman, S. C., et al. 2005, ApJ, 632, 736
Arnaud, K. A. 1996, in ASP Conf. Ser. 101, Astronomical Data Analysis Software and Systems V, ed. G. H. Jacoby & J. Barnes (San Francisco, CA: ASP), 17
Bautz, M. W., Malm, M. R., Baganoff, F. K., et al. 2000, ApJL, 543, L119
Bertin, E., & Arnouts, S. 1996, A&AS, 117, 393
Boquien, M., Burgarella, D., Roehlly, Y., et al. 2019, A&A, 622, A103
Brammer, G. B., van Dokkum, P. G., & Coppi, P. 2008, ApJ, 686, 1503
Bruzual, G., & Charlot, S. 2003, MNRAS, 344, 1000
Burgarella, D., Buat, V., & Iglesias-Páramo, J. 2005, MNRAS, 360, 1413
Calzetti, D., Armus, L., Bohlin, R. C., et al. 2000, ApJ, 533, 682
Calzetti, D., Kinney, A. L., & Storchi-Bergmann, T. 1994, ApJ, 429, 582
Chabrier, G. 2003, PASP, 115, 763
Coe, D., Salmon, B., Bradač, M., et al. 2019, ApJ, 884, 85
da Cunha, E., Walter, F., Smail, I. R., et al. 2015, ApJ, 806, 110
Draper, A. R., & Ballantyne, D. R. 2012, ApJ, 751, 72
Dudzevičiūtė, U., Smail, I., Swinbank, A. M., et al. 2020, MNRAS, 494, 3828
Dunlop, J. S., McLure, R. J., Biggs, A. D., et al. 2017, MNRAS, 466, 861
Egami, E., Rex, M., Rawle, T. D., et al. 2010, A&A, 518, L12
Fabian, A. C., Smail, I., Iwasawa, K., et al. 2000, MNRAS, 315, L8
Fazio, G. G., Hora, J. L., Allen, L. E., et al. 2004, ApJS, 154, 10
Freeman, P. E., Kashyap, V., Rosner, R., & Lamb, D. Q. 2002, ApJS, 138, 185
Fruscione, A., McDowell, J. C., Allen, G. E., et al. 2006, Proc. SPIE, 6270, 62701V
Fujimoto, S., Ouchi, M., Kohno, K., et al. 2018, ApJ, 861, 7
Garmire, G. P., Bautz, M. W., Ford, P. G., Nousek, J. A., & Ricker, G. R. J. 2003, Proc. SPIE, 4851, 28
Geach, J. E., Dunlop, J. S., Halpern, M., et al. 2017, MNRAS, 465, 1789
Gilmour, R., Best, P., & Almaini, O. 2009, MNRAS, 392, 1509

González-López, J., Bauer, F. E., Romero-Cañizales, C., et al. 2017b, A&A, 597, A41
González-López, J., Bauer, F. E., Aravena, M., et al. 2017a, A&A, 608, A138
Hatsukade, B., Kohno, K., Yamaguchi, Y., et al. 2018, PASJ, 70, 105
Hoag, A., Huang, K. H., Treu, T., et al. 2016, ApJ, 831, 182
Hobbs, A., Nayakshin, S., Power, C., & King, A. 2011, MNRAS, 413, 2633
Hodge, J. A., Karim, A., Smail, I., et al. 2013, ApJ, 768, 91
Hopkins, P. F., Hernquist, L., Cox, T. J., & Kereš, D. 2008, ApJS, 175, 356
Hunt, L. K., De Looze, I., Boquien, M., et al. 2019, A&A, 621, A51
Inoue, A. K. 2011, MNRAS, 415, 2920
Jones, A. P., Köhler, M., Ysard, N., Bocchio, M., & Verstraete, L. 2017, A&A, 602, A46
Just, D. W., Brandt, W. N., Shemmer, O., et al. 2007, ApJ, 665, 1004
Kennicutt, R. C. J. 1998, ARA&A, 36, 189
Kennicutt, R. C., Calzetti, D., Aniano, G., et al. 2011, PASP, 123, 1347
Kocevski, D. D., Faber, S. M., Mozena, M., et al. 2012, ApJ, 744, 148
Kocevski, D. D., Hasinger, G., Brightman, M., et al. 2018, ApJS, 236, 48
Kokorev, V., Brammer, G., Fujimoto, S., et al. 2022, ApJS, 263, 38
Komatsu, E., Smith, K. M., Dunkley, J., et al. 2011, ApJS, 192, 18
Kormendy, J., & Ho, L. C. 2013, ARA&A, 51, 511
Laporte, N., Bauer, F. E., Troncoso-Iribarren, P., et al. 2017, A&A, 604, A132
Lehmer, B. D., Alexander, D. M., Bauer, F. E., et al. 2010, ApJ, 724, 559
Lotz, J. M., Koekemoer, A., Coe, D., et al. 2017, ApJ, 837, 97
Luo, B., Bauer, F. E., Brandt, W. N., et al. 2008, ApJS, 179, 19
Lutz, D., Poglitsch, A., Altieri, B., et al. 2011, A&A, 532, A90
Madau, P., & Dickinson, M. 2014, ARA&A, 52, 415
Magorrian, J., Tremaine, S., Richstone, D., et al. 1998, AJ, 115, 2285
Marconi, A., & Hunt, L. K. 2003, ApJL, 589, L21
McMullin, J. P., Waters, B., Schiebel, D., Young, W., & Golap, K. 2007, in ASP Conf. Ser. 376, Astronomical Data Analysis Software and Systems XVI, ed. R. A. Shaw, F. Hill, & D. J. Bell (San Francisco, CA: ASP), 127
Mineo, S., Gilfanov, M., Lehmer, B. D., Morrison, G. E., & Sunyaev, R. 2014, MNRAS, 437, 1698
NASA High Energy Astrophysics Science Archive Research Center (HEASARC) 2014, HEAsoft: Unified Release of FTOOLS and XANADU, Astrophysics Source Code Library, ascl:1408.004
Nobuta, K., Akiyama, M., Ueda, Y., et al. 2012, ApJ, 761, 143
Noll, S., Burgarella, D., Giovannoli, E., et al. 2009, A&A, 507, 1793
Page, M. J., Symeonidis, M., Vieira, J. D., et al. 2012, Natur, 485, 213
Peca, A., Cappelluti, N., Urry, C. M., et al. 2023, ApJ, 943, 162
Postman, M., Coe, D., Benítez, N., et al. 2012, ApJS, 199, 25
Ricci, C., Bauer, F. E., Treister, E., et al. 2017, MNRAS, 468, 1273

Ricci, C., Privon, G. C., Pfeifle, R. W., et al. 2021, MNRAS, 506, 5935
Rieke, G. H., Young, E. T., Engelbracht, C. W., et al. 2004, ApJS, 154, 25
Rujopakarn, W., Dunlop, J. S., Rieke, G. H., et al. 2016, ApJ, 833, 12
Sanders, D. B., & Mirabel, I. F. 1996, ARA&A, 34, 749
Schawinski, K., Treister, E., Urry, C. M., et al. 2011, ApJL, 727, L31
Setoguchi, K., Ueda, Y., Toba, Y., & Akiyama, M. 2021, ApJ, 909, 188
Silva, L., Granato, G. L., Bressan, A., & Danese, L. 1998, ApJ, 509, 103
Smail, I., Ivison, R. J., & Blain, A. W. 1997, ApJL, 490, L5
Smail, I., Ivison, R. J., Blain, A. W., & Kneib, J. P. 2002, MNRAS, 331, 495
Soucail, G., Kneib, J. P., Bézecourt, J., et al. 1999, A&A, 343, L70
Speagle, J. S., Steinhardt, C. L., Capak, P. L., & Silverman, J. D. 2014, ApJS, 214, 15
SSC & IRSA 2020, Spitzer Enhanced Imaging Products
Stach, S. M., Smail, I., Swinbank, A. M., et al. 2018, ApJ, 860, 161
Stach, S. M., Dudzevičiūtė, U., Smail, I., et al. 2019, MNRAS, 487, 4648
Stalevski, M., Fritz, J., Baes, M., Nakos, T., & Popović, L. Č. 2012, MNRAS, 420, 2756
Stalevski, M., Ricci, C., Ueda, Y., et al. 2016, MNRAS, 458, 2288
Steinhardt, C. L., Jauzac, M., Acebron, A., et al. 2020, ApJS, 247, 64
Sun, F., Egami, E., Fujimoto, S., et al. 2022, ApJ, 932, 77
Sun, F., Egami, E., Rawle, T. D., et al. 2021, ApJ, 908, 192
Takata, T., Sekiguchi, K., Smail, I., et al. 2006, ApJ, 651, 713
Toba, Y., Liu, T., Urrutia, T., et al. 2022, A&A, 661, A15
Ueda, Y., Akiyama, M., Hasinger, G., Miyaji, T., & Watson, M. G. 2014, ApJ, 786, 104
Ueda, Y., Hatsukade, B., Kohno, K., et al. 2018, ApJ, 853, 24
Ueda, Y., Watson, M. G., Stewart, I. M., et al. 2008, ApJS, 179, 124
Umehata, H., Tamura, Y., Kohno, K., et al. 2015, ApJL, 815, L8
Vasudevan, R. V., & Fabian, A. C. 2007, MNRAS, 381, 1235
Wang, S., Liu, J., Qiu, Y., et al. 2016, ApJS, 224, 40
Wang, S. X., Brandt, W. N., Luo, B., et al. 2013, ApJ, 778, 179
Weiß, A., Kovács, A., Coppin, K., et al. 2009, ApJ, 707, 1201
Weisskopf, M. C., Brinkman, B., Canizares, C., et al. 2002, PASP, 114, 1
Willingale, R., Starling, R. L. C., Beardmore, A. P., Tanvir, N. R., & O'Brien, P. T. 2013, MNRAS, 431, 394
Yamada, S., Ueda, Y., Tanimoto, A., et al. 2021, ApJS, 257, 61
Yamada, S., Ueda, R., Herrera-Endoqui, M., et al. 2023, arXiv:2301.03613
Yamaguchi, Y., Kohno, K., Hatsukade, B., et al. 2020, PASJ, 72, 69
Yang, G., Boquien, M., Buat, V., et al. 2020, MNRAS, 491, 740
Yang, G., Boquien, M., Brandt, W. N., et al. 2022, ApJ, 927, 192
Yutani, N., Toba, Y., Baba, S., & Wada, K. 2022, ApJ, 936, 118